

# Enhancing thermoelectric properties of spinel ZnFe<sub>2</sub>O<sub>4</sub> by Ni substitution through electron hopping mechanism



Navya John <sup>a</sup>, Nithya Davis <sup>a</sup>, T. Gokul Raja <sup>a</sup>, J.C. Roshan <sup>a</sup>, Shamima Hussain <sup>b</sup>, Sebin Devasia <sup>a</sup>, Bhuvanesh Srinivasan <sup>c</sup>, Anuradha M. Ashok <sup>a,\*</sup>

<sup>a</sup> Functional Materials Laboratory, PSG Institute of Advanced Studies, Peelamedu, Coimbatore, 641004, T. N., India

<sup>b</sup> UGC-DAE Consortium for Scientific Research, Kalpakkam Node Kokilamedu, 603104, T. N., India

<sup>c</sup> Department of Metallurgical and Materials Engineering, Indian Institute of Technology Madras, Chennai, 600036, T. N., India

## ARTICLE INFO

Handling Editor: Dr P. Vincenzini

### Keywords:

Spins  
Sol-gel processes  
Electrical conductivity  
Thermal conductivity

## ABSTRACT

The prime goal of this novel work is to investigate the efficacy of spinel zinc ferrite as a thermoelectric material and its performance enhancement for high temperature applications. Zn<sub>1-x</sub>Ni<sub>x</sub>Fe<sub>2</sub>O<sub>4</sub> (0 ≤ x ≤ 0.2) were prepared by sol-gel method and their structural, morphological, and thermoelectric behaviours were examined as functions of composition and temperature. Among the studied compositions, Zn<sub>0.8</sub>Ni<sub>0.2</sub>Fe<sub>2</sub>O<sub>4</sub> exhibits the highest electrical conductivity ( $\sigma$ ) of 49.83 S/m, the largest power factor of 6.66  $\mu$ W/mK<sup>2</sup>, and the lowest thermal conductivity ( $\kappa$ ) of 0.36 W/mK at 947 K, thus extending to an overall enhancement in the thermoelectric figure of merit ( $zT$ ). Conduction through electron hopping is proven to be the main driving force for the enhancement in electrical and thus thermoelectric properties. Results reveal that thermoelectric properties of ZnFe<sub>2</sub>O<sub>4</sub> can potentially be enhanced by the doping Ni at Zn site and opens up an exciting opportunity for the utilization of this spinel ferrite as a novel thermoelectric material for applications involving elevated temperatures.

## 1. Introduction

Increase in global demand for sustainable energy production drives the requirement to create new technologies in order to address the energy crisis, climate change, and global warming. Energy generation through thermoelectrics (TE) is considered as an exceptionally auspicious method to reap energy from waste heat and natural heat resources. This method will excavate huge amount of quiescent energy in the form of waste heat for power generation which otherwise will devote to environmental issues. Thermoelectric energy conversion is of great significance because it directly converts the thermal energy with a temperature gradient into electrical energy. The functioning of thermoelectric material and its performance is evaluated through Figure of merit ( $zT$ ) and it can be quantified using Equation (1).

$$zT = \frac{S^2\sigma}{\kappa} T \quad (1)$$

Where,  $S$ ,  $\sigma$ ,  $T$  and  $\kappa$  represent Seebeck coefficient, electrical conductivity, temperature and thermal conductivity respectively [1]. Strategies that can be adopted to achieve good thermoelectric properties are

optimization of power factor ( $S^2\sigma$ ) and reduction of thermal conductivity ( $\kappa$ ) which contains both the electronic and phononic contributions [2]. The use of traditional TE materials, such as Bi<sub>2</sub>Te<sub>3</sub>, skutterudites, and chalcogenides are limited due to their harmful effects to the environment, which prevent their large-scale applications. These materials have high  $zT$  but are toxic, rare on earth, contain heavy elements, and have poor chemical and thermal stability at higher temperatures [3]. Nevertheless, oxide-based thermoelectric materials have advantageous qualities such as non-toxicity, abundance in the earth, and stability at high temperatures, which results in applications that are indestructible [4].

Zinc oxide is a well-known thermoelectric material [5]. Because of large carrier mobility and less electro negativity difference between Zn and O, ZnO is becoming more and more appealing as a high temperature thermoelectric material. With the help of nano-structuring, doping, co-doping and composite making with graphene, remarkable improvement of thermoelectric performance in ZnO has been achieved with the highest figure of merit of 2.4 at 500 K for ZnO/graphene hetero structure [6–8]. Herein, an effort is made to investigate ZnFe<sub>2</sub>O<sub>4</sub> (ZFO), the complex oxide form of ZnO with the multivalent transition element Fe

\* Corresponding author.

E-mail address: [anu@psgias.ac.in](mailto:anu@psgias.ac.in) (A.M. Ashok).

for thermoelectric applications. The scientific community views the spinel ferrite  $ZnFe_2O_4$  as extremely intriguing due to its exceptional structural, electrical, and magnetic properties, as well as its capacity to form stable complexes under different preparation conditions and usability at extreme conditions [9]. More specifically,  $ZnFe_2O_4$  is extensively studied for the conversion of solar energy, photocatalysis, and photochemical hydrogen production [10,11]. The functional property enhancement in  $ZnFe_2O_4$  has been attempted using several methods. The replacement of some of  $Fe^{3+}$  with  $Ti^{4+}$  increases the carrier concentration of  $ZnFe_2O_4$ , resulting in an eight-fold increment in the photocurrent of the  $Ti$ -doped  $ZnFe_2O_4$  photo anode ( $0.35 \text{ mA cm}^{-2}$ ) [12].  $La^{3+}$  substituted zinc ferrite nanoparticles with the composition  $ZnFe_{1.95}La_{0.05}O_4$  and partial spinel structure were found to exhibit very good magnetization of  $7.6 \text{ emu/g}$  even by the replacement of highly magnetic  $Fe^{3+}$  cation by non-magnetic  $La^{3+}$  cation [13]. Due to the single oxidation state of  $Cr$  ( $Cr^{3+}$ ),  $ZnCr_xFe_{2-x}O_4$  exhibits lower conductivity than parent  $ZnFe_2O_4$  because it hinders electron hopping between ferrous and ferric ions, rather than enhancing conduction [9]. Ni-doped zinc ferrite is a promising *n*-type material having an inverse spinel structure with  $Ni^{3+}$  replacing  $Zn^{2+}$  at the tetrahedral site and multivalent (3+ and 2+) Fe occupying the octahedral site [14].

$Ni_{0.5}Zn_{0.5}Fe_2O_4$  is reported as a potential material for the production of microwave absorbers because its dielectric constants drop with frequency demonstrating dielectric dispersion at low frequencies [15]. The thermoelectric properties of zinc ferrites, however, have not yet been reported. Among many methods to improve  $zT$ , doping multivalent element like Ni is expected to not only effectively enhance electrical conductivity through improved carrier concentration and mobility, but also reduce thermal conductivity by phonon scattering at the substitutional site. Therefore, in this study the thermoelectric properties of Ni-substituted zinc ferrite ( $Ni_xZn_{1-x}Fe_2O_4$ ) synthesized by using sol-gel method were examined and the influence of Ni doping in the structural, morphological, and thermoelectric properties is reported.

## 2. Materials and methods

$Zn_{1-x}Ni_xFe_2O_4$  ( $0 \leq x \leq 0.2$ ) was synthesized by using sol-gel method. The stoichiometric ratios of the precursors  $Zn(NO_3)_2 \cdot 6 H_2O$  (Hi-Media),  $Fe(NO_3)_3 \cdot 9 H_2O$  (Merck), and  $Ni(NO_3)_2 \cdot 6H_2O$  (Loba chemie) corresponding to each composition were separately added into 100 ml of distilled water. For the formation of sol, polyethylene glycol was added, which acts as a complexing agent. In addition, citric acid was added in 1:1 ratio to the mixture, where citric acid helps in the homogenous distribution of the constituents and leads to the segregation of metal ions. The solution was heated and stirred at a moderate temperature to form a viscous gel. The gel was heated again in a hot air oven at  $100^\circ C$  for 12 h to evaporate water and obtain a sponge-like product. At this stage, the gel forms a covalent network with the cations blocked at a particular position. The gel formed was calcined at  $1100^\circ C$  for 2 h at a heat rate of  $10^\circ C/\text{min}$  in a muffle furnace. The calcined powders were pressed into circular disc shaped pellets of diameter 13 mm and thickness 2 mm with a pressure 10 tons and later sintered at  $1200^\circ C$  for 1 h in  $N_2$  environment in a tubular furnace. Identification of the calcination temperature of the intermediate reaction mixture was done using simultaneous thermal analyser (NETZSCH STA 449 F3 Jupiter, Germany). Scanning electron microscopy (SEM, Carl Zeiss EVO 18, Germany) was performed to study the morphology of the compositions. X-ray diffraction (XRD) was performed for crystallographic analysis using Empyrean X-ray diffractometer (Malvern PANalytical, Netherland) with  $Cu-K\alpha$  radiation ( $\lambda = 1.54 \text{ \AA}$ ). X-ray Photoelectron Spectroscopy (PHI – VERSAPROBE III) was carried out to understand the surface elemental composition and oxidation states. In depth morphological and crystallographic characterization of the samples were performed using JEOL JEM 2100 (Japan) high-resolution transmission electron microscope at an accelerating voltage of 200 kV. Ulvac Riko ZEM – 310 Seebeck coefficient/electrical resistance measurement system was used to perform

thermoelectric property analysis. Thermal conductivity analysis data was obtained using laser flash analysis method (Netzsch LFA 427, Germany). The room temperature carrier concentration and mobility of the sintered pellets with dimension  $1.5 \times 1.5 \text{ cm}$  were measured using Ecopia HMS 3000 Hall measurement system.

Density functional theory (DFT) calculations of  $ZnFe_2O_4$  and Ni-doped  $ZnFe_2O_4$  were performed within the framework of the open source Quantum ESPRESSO package [10.1088/0953-8984/21/39/395502, 10.1088/1361-648X/AA8F79] and BURAI graphical user interface. Initially, a self-consistent field (SCF) convergence test was performed to obtain the plane wave kinetic energy cut off, charge density cut off, and k-mesh as 60 Ry, 360 Ry, and  $7 \times 7 \times 7$ , respectively. The convergence criterion for forces was  $10^{-7} \text{ Ry/Bohr}$ . Here, the electron-ion interactions were described by PAW (Kresse-Joubert) pseudo potential with Perdew-Burke-Ernzerhof (GGA) functional.

## 3. Results and discussions

### 3.1. Thermal analysis

Fig. 1 shows the weight loss profile of the intermediate gel obtained during the synthesis of  $ZnFe_2O_4$  as a function of temperature. It is evident that the TGA curve exhibits two major weight losses in the temperature ranges of  $50$ – $200^\circ C$  and  $200$ – $400^\circ C$ . The initial major weight loss of 12 % is owing to the evaporation of adsorbed water molecules and the removal of unreacted organic residues that still remain in the sample, which also corresponds to a small peak in the DSC curve. The second weight loss of 26 % is due to the removal of interlayer water molecules and the conversion of nitrates into ferrites. This is also evident from the relatively intense exothermic peak in the DSC curve [16]. In the temperature range of  $400^\circ C$ – $1200^\circ C$ , there is no significant weight loss, indicating the formation of a stable final composition. Crystallization and formation of the spinel phase starts after  $400^\circ C$ . Horizontal TG curve after  $400^\circ C$  also indicates the stability of the compound till  $1100^\circ C$ . Based on this observation the dried gel was calcined at  $1100^\circ C$  for 2 h.

### 3.2. Structural characterizations

XRD data in Fig. 2(a) reveals the information regarding the crystal structure and phase purity of  $ZnFe_2O_4$ ,  $Zn_{0.9}Ni_{0.1}Fe_2O_4$  and  $Zn_{0.8}Ni_{0.2}Fe_2O_4$  sintered at  $1200^\circ C$  for 1 h in  $N_2$  atmosphere. The peaks are indexed according to the reported cubic crystal structure of  $ZnFe_2O_4$  with space group  $Fd\bar{3}m$  (#227) and cell dimension  $8.4380 \text{ \AA}$  (ICDD NO: 01-073-3824). No change in the patterns after doping, and absence of peaks corresponding to any secondary phases indicates the successful

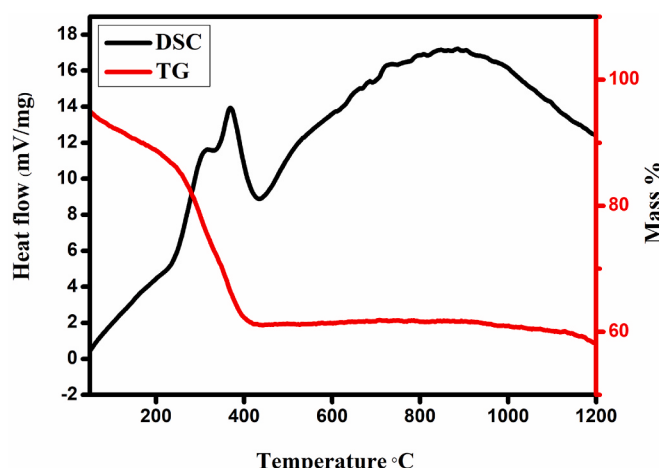
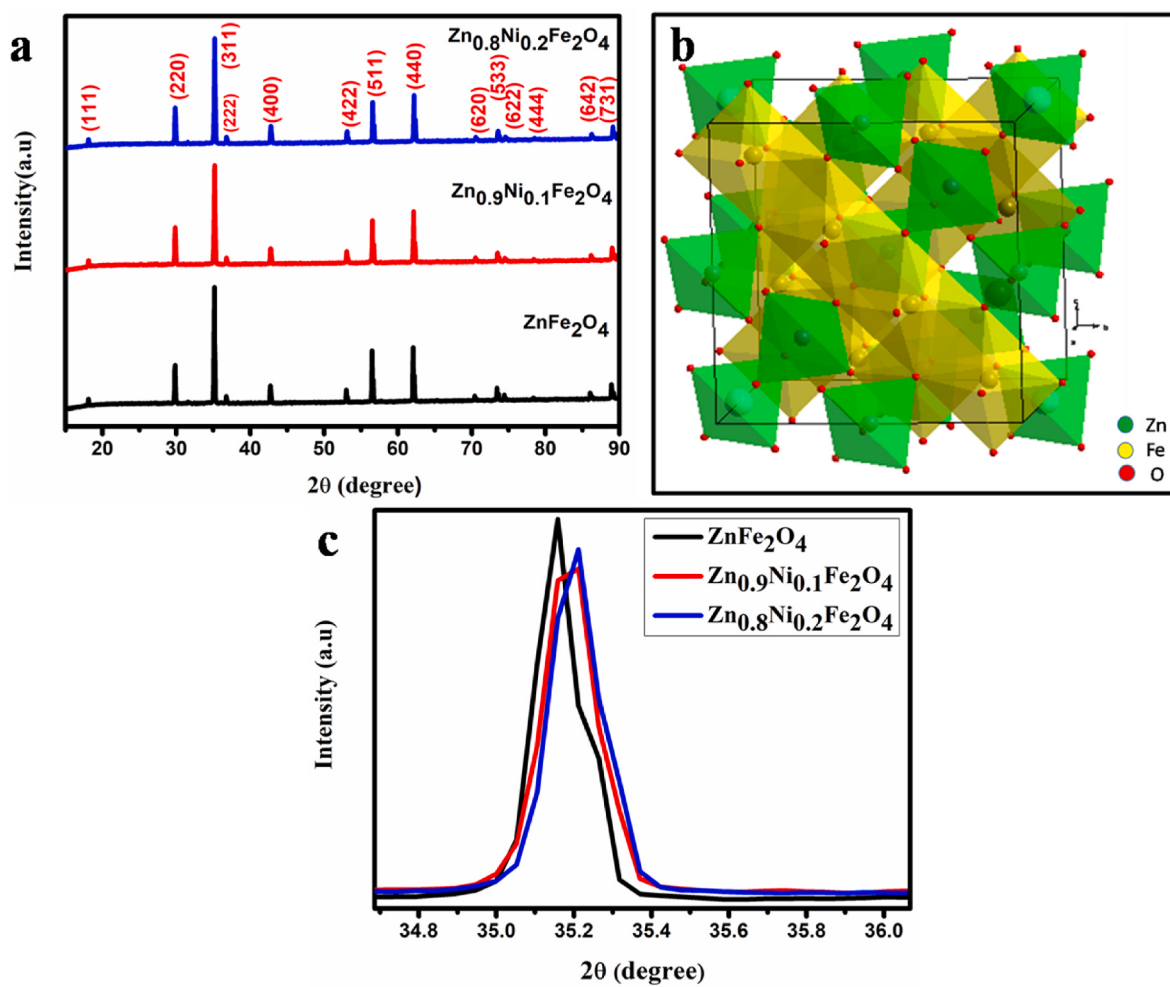


Fig. 1. TG–DSC analysis of intermediate gel of  $ZnFe_2O_4$ .



**Fig. 2.** (a) X-ray diffractogram taken from parent and Ni doped  $\text{ZnFe}_2\text{O}_4$  sintered pellets,(b) crystal structure of  $\text{ZnFe}_2\text{O}_4$ and (c) enlarged peaks corresponding to (311) crystal plane.

substitution of the dopants in the parent crystal lattice. As depicted in Fig. 2(c), a right shift in peak positions is occurred due to the lattice contraction because of smaller Ni (ionic radius-0.55 Å) replacing the larger Zn (ionic radius –0.6 Å) ions.

Using the X'pert Highscore plus software, Rietveld analysis of the studied compositions was performed (details are provided in supplementary data S1).The experimental diffractograms were matched with cubic Franklinite ( $\text{Fe}_{16.21}\text{Zn}_{7.79}\text{O}_{32.00}$ ) crystal structure with space group  $Fd\bar{3}m$  and cell dimension 8.4560 Å (COD 96-900-2489). Table 1 shows the refined cell parameters of studied compositions which attributes to the contraction in lattice sites via doping of Ni in the Zn positions.

Using Scherrer calculator from X'pert Highscore Plus software, the average crystallite size and strain were calculated and the values are indicated in Table 1.The data reveals that doping of Ni results in decrease in crystallite size of  $\text{ZnFe}_2\text{O}_4$  and the reduction in crystallite size increases with increase in Ni content. A noticeable increase in lattice strain can also be observed in Ni doped samples owing to the

replacement of larger Zn ions by smaller Ni ions. Among all the compositions, $\text{Zn}_{0.8}\text{Ni}_{0.2}\text{Fe}_2\text{O}_4$  showed the lowest crystallite size and the highest strain.

To understand the surface elemental composition and oxidation states of different elements present in  $\text{Zn}_{1-x}\text{Ni}_x\text{Fe}_2\text{O}_4$  ( $0 \leq x \leq 0.2$ ) pellets, XPS analysis of  $\text{Zn}_{0.8}\text{Ni}_{0.2}\text{Fe}_2\text{O}_4$  was performed and the results are depicted in Fig. 3(a-d).Fig. 3(a) shows the measured XPS spectra of Zn 2p core-level of  $\text{Zn}_{0.8}\text{Ni}_{0.2}\text{Fe}_2\text{O}_4$  pellet.The spectra consist of two peaks corresponding to Zn 2p<sub>3/2</sub> and Zn 2p<sub>1/2</sub> at 1022.1 eV and 1045.1 eV respectively, which indicates that Zn exists mainly in +2 oxidation state [17,18].

The Fe 2p spectra of the  $\text{Zn}_{0.8}\text{Ni}_{0.2}\text{Fe}_2\text{O}_4$  shown in Fig. 3(b) exhibits the characteristic doublet located at 710.4 eV (Fe 2p<sub>3/2</sub>) and 723.8 eV (Fe 2p<sub>1/2</sub>).The deconvolution of Fe 2p<sub>3/2</sub> spectra shows three peaks centred at 709.8 eV, 711.2 eV corresponding to  $\text{Fe}^{2+}$  state and third peak at 713.6 eV corresponding to  $\text{Fe}^{3+}$  valence state. Additionally, a satellite peak at a binding energy of about 715–718 eV is identified for the main

**Table 1**  
Refined cell parameters of all compositions.

Compound	Crystal system and space group	Cell dimension (Å)	Rwp	$\chi^2$	Average crystallite size(nm)	Lattice strain
$\text{Fe}_{16.21}\text{Zn}_{7.79}\text{O}_{32}$	Cubic $Fd\bar{3}m$ (#227)	8.4560				
$\text{ZnFe}_2\text{O}_4$		8.4426	2.4975	2.2385	1119	0.103
$\text{Zn}_{0.9}\text{Ni}_{0.1}\text{Fe}_2\text{O}_4$		8.4344	2.3974	2.2338	969	0.116
$\text{Zn}_{0.8}\text{Ni}_{0.2}\text{Fe}_2\text{O}_4$		8.4263	1.7967	1.7967	959	0.116

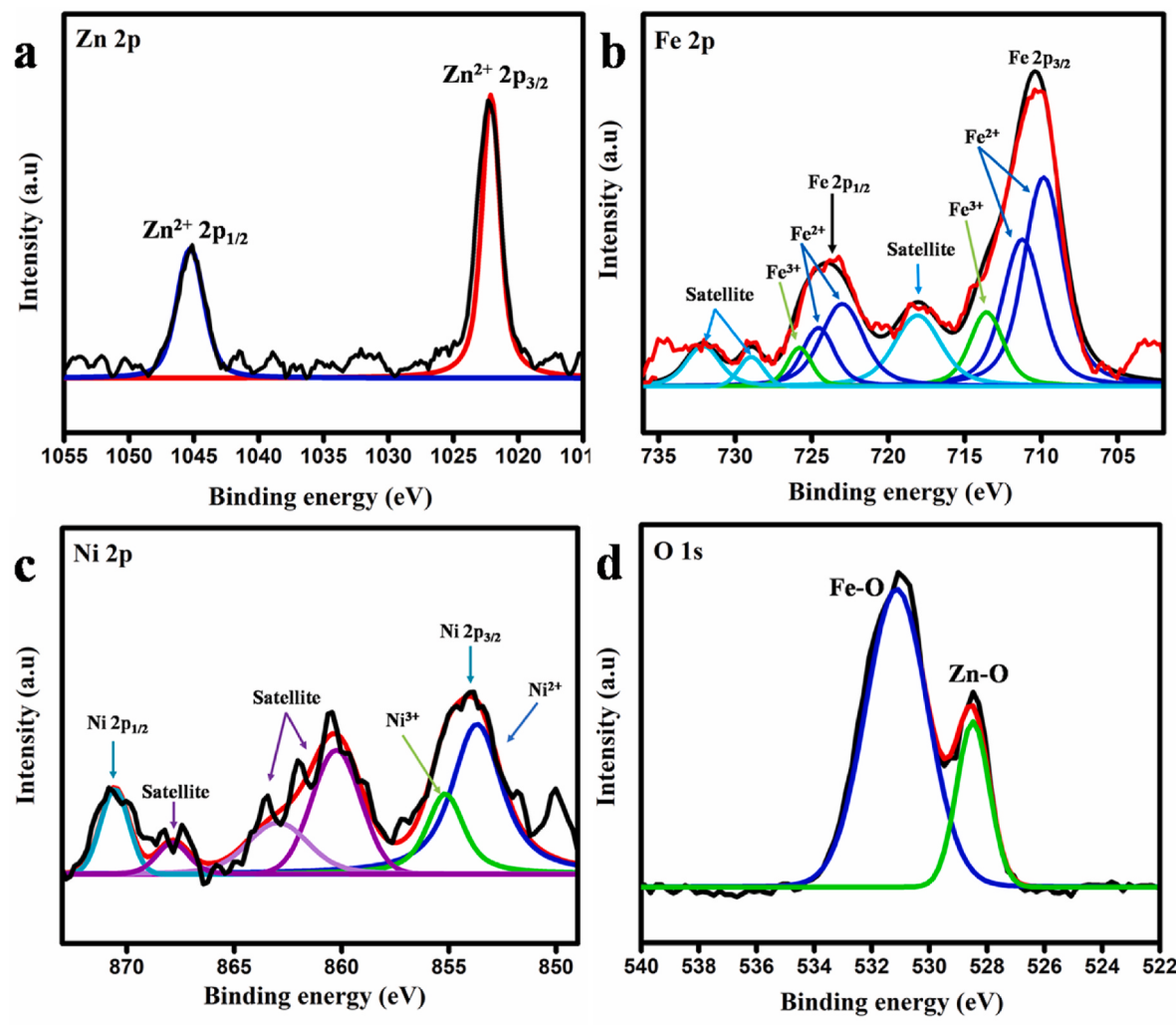


**Fig. 3.** High resolution XPS spectra of  $\text{Zn}_{0.8}\text{Ni}_{0.2}\text{Fe}_2\text{O}_4$  (a) Zn 2p, (b) Fe 2p, (c) Ni 2p, and (d) O 1s.

peak of Fe2p multiplet. Deconvoluting the second major peak corresponding to Fe 2p<sub>1/2</sub> also revealed three peaks centred at 723.0 eV, 724.6 eV and 725.8 eV, which are associated to Fe<sup>2+</sup> state for the first two peaks and last one for Fe<sup>3+</sup> state respectively. Furthermore, two satellite peaks were obtained at 729.0 eV and 732.0 eV. Thus, these spectral results clearly confirm the presence of iron in, both its trivalent and divalent states in  $\text{Zn}_{0.8}\text{Ni}_{0.2}\text{Fe}_2\text{O}_4$ . [19,20].

From Figure 3 (c), it is observed that characteristic doublet of Ni 2p XPS spectra located at 853.8 eV is for Ni 2p<sub>3/2</sub> and 870.8 eV is for Ni 2p<sub>1/2</sub>. Deconvolution of Ni 2p<sub>3/2</sub> spectra resulted in two peaks centred at 853.6 eV and 855.2 eV, which corresponds to Ni<sup>2+</sup> and Ni<sup>3+</sup> valence states [21]. Additionally, satellite peaks showing broad characteristics at 861 eV and 867.8 eV are identified for the main peak of Ni2p multiplet. Thus, these spectral results clearly confirm the presence of Ni with both its trivalent and divalent state in  $\text{Zn}_{0.8}\text{Ni}_{0.2}\text{Fe}_2\text{O}_4$ . The existence of multivalent state of Fe and Ni in  $\text{Zn}_{0.8}\text{Ni}_{0.2}\text{Fe}_2\text{O}_4$  opens up the possibility of electron transfer between Ni and Fe ions ( $\text{Fe}^{3+} + \text{Ni}^{2+} \leftrightarrow \text{Fe}^{2+} + \text{Ni}^{3+}$ ) [22].

The high-resolution O1s spectra displayed in Fig. 3(d), can be fitted by two peaks at 528.4 and 531.0 eV, corresponding to lattice oxygen binding with Zn and Fe in the metal–oxygen frame work respectively [23,24].

### 3.3. Morphological studies

Fig. 4 shows the scanning electron micrographs of the pellets of  $\text{ZnFe}_2\text{O}_4$ ,  $\text{Zn}_{0.9}\text{Ni}_{0.1}\text{Fe}_2\text{O}_4$  and  $\text{Zn}_{0.8}\text{Ni}_{0.2}\text{Fe}_2\text{O}_4$  sintered at 1200°C for 1 h in N<sub>2</sub> atmosphere. The micrographs reveal the formation of dense and compact pellets with fine grains in micrometer range arranged uniformly with distinct boundaries. Grain boundaries are thought to be highly effective in reducing lattice thermal conductivity by obstructing the phonon conduction without creating significant change on electron movement [25]. However, the nickel doped samples appear to be less dense when compared to the undoped ZFO. Density measured via mass/volume ratio and theoretical densities for each sample are listed in Table 2. Owing to the higher porosity as revealed by SEM images, a decrease in density of the Ni doped samples can be observed.

HR-TEM images of the pellets  $\text{ZnFe}_2\text{O}_4$ ,  $\text{Zn}_{0.9}\text{Ni}_{0.1}\text{Fe}_2\text{O}_4$ , and  $\text{Zn}_{0.8}\text{Ni}_{0.2}\text{Fe}_2\text{O}_4$  sintered at 1200°C for 1 h in N<sub>2</sub> atmosphere are shown in Fig. 5. Thinner areas of lower magnification images of the compounds in Fig. 5(a1, b1 and c1) have been used to take high resolution images shown in Fig. 5(a2, b2 and c2). The presence of discrete lattice fringes in HR-TEM images confirms that each grains are composed of single crystals oriented along specific directions/planes as also confirmed by the spot type SAED patterns (Fig. 5(a3, b3 and c3)). The SAED patterns are interpreted based on the crystal structure obtained from XRD results.

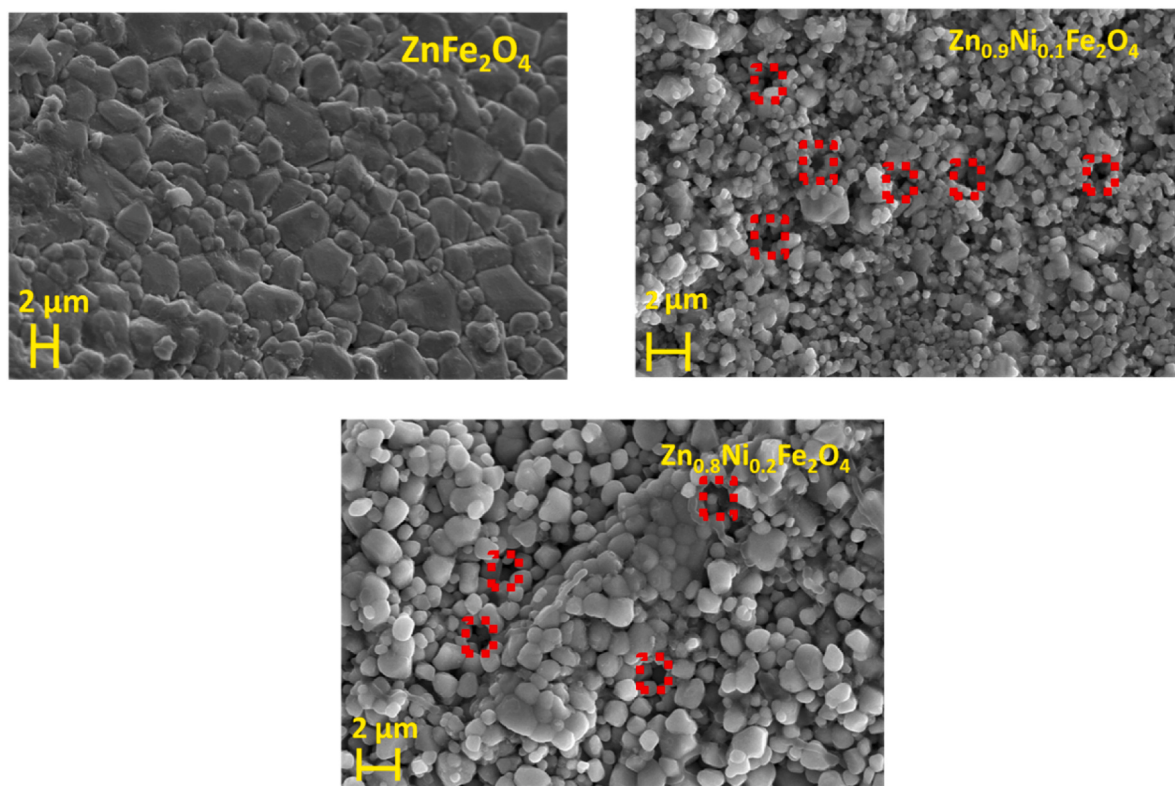


**Fig. 4.** SEM micrographs of  $\text{ZnFe}_2\text{O}_4$  and Ni doped  $\text{ZnFe}_2\text{O}_4$  pellets.

**Table 2**  
Density values of various sintered pellets.

Composition	Density (g/cm <sup>3</sup> )	Theoretical density(g/cm <sup>3</sup> )	Relative density
$\text{ZnFe}_2\text{O}_4$	3.756	5.323	70.56
$\text{Zn}_{0.9}\text{Ni}_{0.1}\text{Fe}_2\text{O}_4$	3.483	5.324	65.42
$\text{Zn}_{0.8}\text{Ni}_{0.2}\text{Fe}_2\text{O}_4$	3.343	5.324	62.79

#### 3.4. Transport properties

To further investigate mechanism underlying the thermoelectric properties, the carrier concentrations ( $n$ ) and carrier mobilities ( $\mu$ ) of the studied compositions were recorded at room temperature through Hall measurement. As shown in Fig. 6(a), carrier concentration values are of similar range for  $\text{ZnFe}_2\text{O}_4$ ,  $\text{Zn}_{0.9}\text{Ni}_{0.1}\text{Fe}_2\text{O}_4$  and  $\text{Zn}_{0.8}\text{Ni}_{0.2}\text{Fe}_2\text{O}_4$ , which are  $1.331 \times 10^{13}$ ,  $1.281 \times 10^{13}$ , and  $1.179 \times 10^{13} \text{ cm}^{-3}$  respectively. Contrary to the initial assumption, a decrease in carrier concentration on Ni doping and further decrease with increasing Ni content can be observed here. This could be possibly due to the utilization of electrons belonging to some of the trivalent Ni ions to convert some of the  $\text{Fe}^{2+}$  ions into  $\text{Fe}^{3+}$  at room temperature so that overall number of free charge carriers gets reduced. Consequently, significantly higher mobility exhibited by  $\text{Zn}_{0.8}\text{Ni}_{0.2}\text{Fe}_2\text{O}_4$  when compared to the undoped  $\text{ZnFe}_2\text{O}_4$ , is attributed to its lower carrier concentration and also presence of smaller Ni atoms in larger Zn positions in the cation sub lattice. Because of the magnetic property and low room temperature conductivity it is difficult to perform transport property analysis of these materials using Hall measurements [26]. Therefore, further electrical property analyses were performed using the simultaneous high temperature electrical resistivity and Seebeck measurement system [27].

#### 3.5. Electrical property analysis

From the conductivity data in Fig. 7 (a), it is evident that all the sintered pellets exhibit semiconducting behaviour and the conductivity strongly depends on temperature. Additionally, it is apparent that the presence of Ni significantly improves the electrical properties of  $\text{ZnFe}_2\text{O}_4$ . The enhancement in electrical conductivity could be due to the collective contribution of several transport pathways. One of the transport mechanisms is electron hopping due to the exchange of electrons between the cations in the octahedral site (B site) of the same element (Fe) that exhibits more than one valence states [28]. In addition, the extra carriers provided by the higher-valent dopant ( $\text{Ni}^{3+}$  in  $\text{Zn}^{2+}$  site) and those from the vacant oxygen sites also contribute to conduction through the normal route via chains of cationic polyhedra at higher temperatures. Consequently, when compared to undoped  $\text{ZnFe}_2\text{O}_4$ , Ni-doped  $\text{ZnFe}_2\text{O}_4$  exhibits better electrical conductivity in all studied temperature ranges, which increases with increasing dopant concentration. Remarkably, it should be mentioned that the improvement in electrical conductivity in  $\text{Zn}_{1-x}\text{Ni}_x\text{Fe}_2\text{O}_4$  is only up to  $x = 0.2$ , beyond which the resistance of the sample substantially increases to a level which is beyond the measurement capability of the equipment. The primary motivation for selecting nickel as a dopant is to increase electrical conductivity by electron hopping between the transition elements Fe and Ni at both the octahedral and tetrahedral sites. The addition of impurities or the replacement of zinc with elements such as nickel that have variable oxidation states affect the concentration and mobility of charge carriers and influence the overall conductivity. Since both dopant and B cation are multivalent there are several possibilities of electron hopping facilitating electrical conductivity. The electron hopping at the octahedral sites in between the  $\text{Fe}^{2+}$  and  $\text{Fe}^{3+}$  is as shown in (2).



At tetrahedral site,  $\text{Zn}^{2+}$  replaced by Ni with variable oxidation states

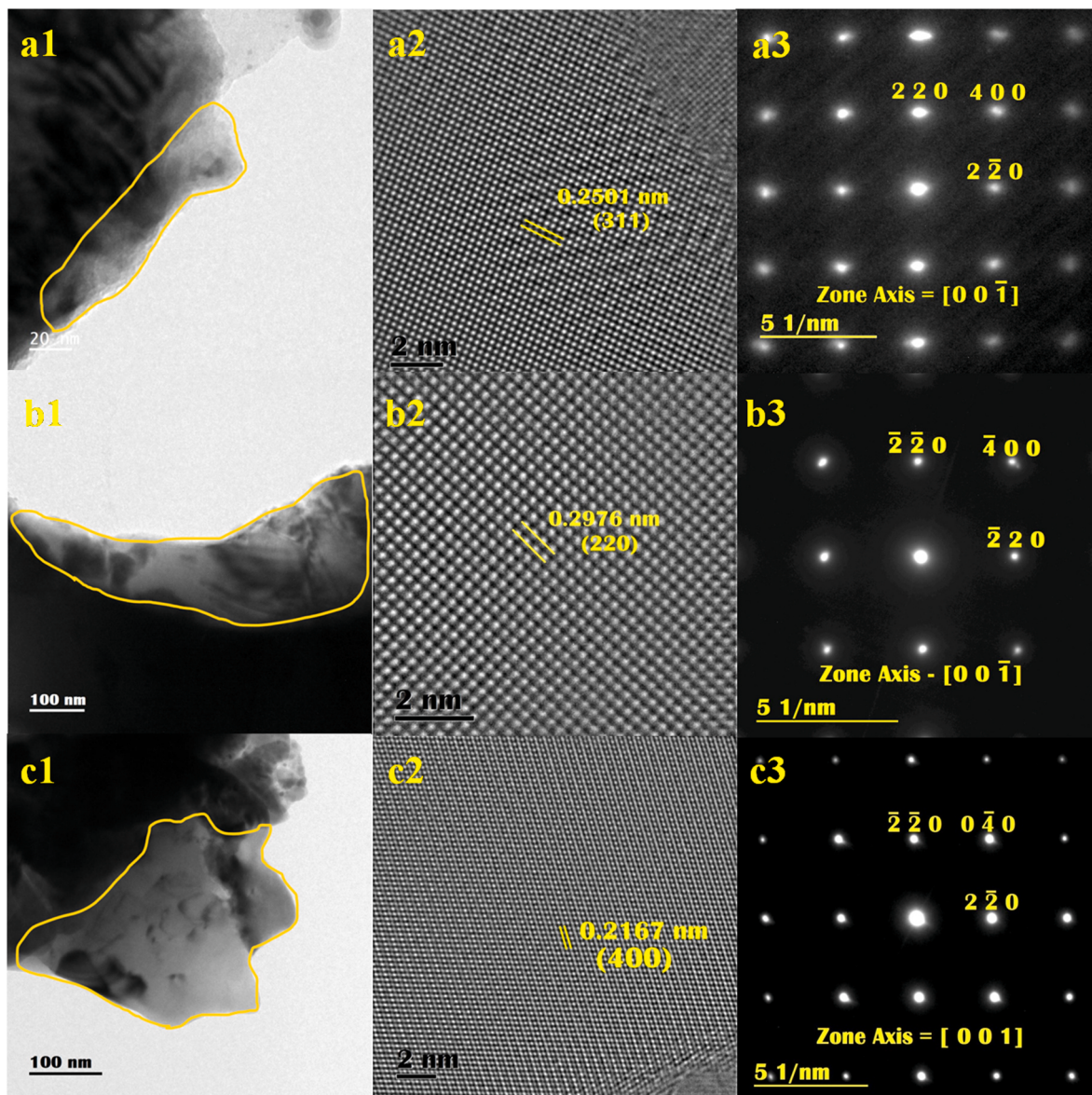


**Fig. 5.** HRTEM images of sintered ZnFe<sub>2</sub>O<sub>4</sub>, Zn<sub>0.9</sub>Ni<sub>0.1</sub>Fe<sub>2</sub>O<sub>4</sub> and Zn<sub>0.8</sub>Ni<sub>0.2</sub>Fe<sub>2</sub>O<sub>4</sub>, a1, b1 and c1 at lower magnification, a2, b2 and c2 high resolution images, a3, b3 and c3 SAED patterns.

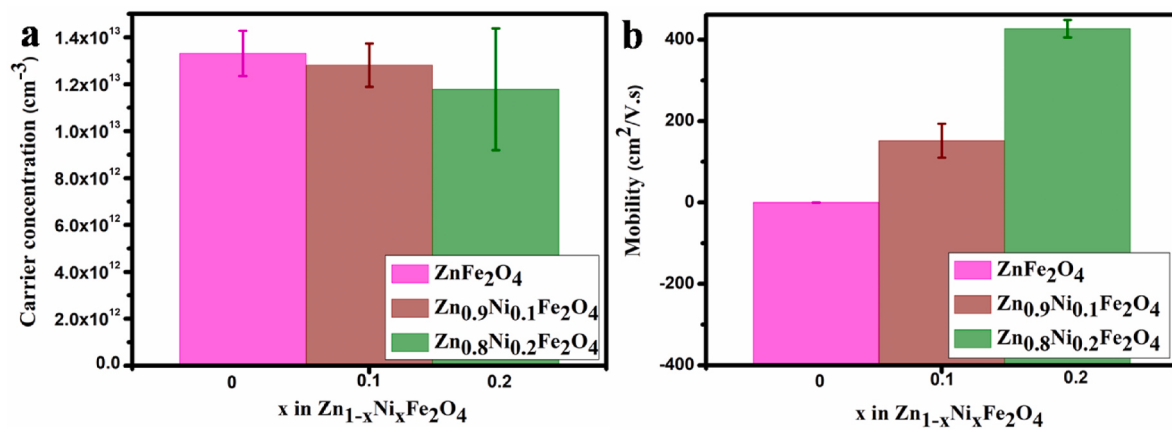


**Fig. 6.** (a) Carrier concentration and (b) Mobility of Spinel ferrite Zn<sub>1-x</sub>Ni<sub>x</sub>Fe<sub>2</sub>O<sub>4</sub> (0 ≤ x ≤ 0.2) at room temperature.

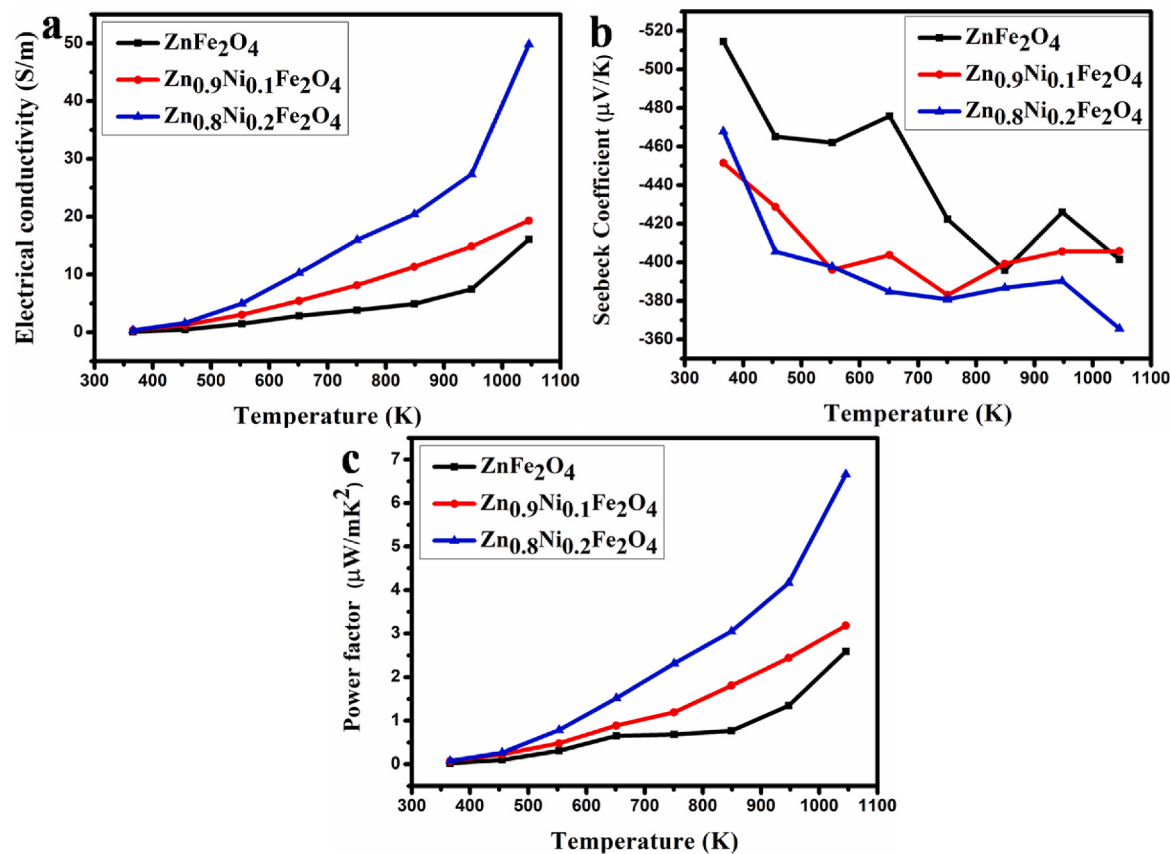


Fig. 7. Temperature dependent (a) Electrical conductivity, (b) Seebeck coefficient and (c) Power factor as a function of temperature of studied compounds.

is involved in hopping process as shown in (3)



However, due to low dopant concentration the probability of the scenario mentioned in (3) is very low. Instead, hopping between Fe and Ni between tetrahedral and octahedral sites is possible with electron transfer mechanism mentioned in (4).



The Seebeck coefficient values of all the compositions as a function of temperature are showed in Fig. 7(b). The negative value of the Seebeck coefficient proves that electrons are the major charge carriers in these compounds. Owing to the lowest carrier concentration among all studied compositions, ZnFe<sub>2</sub>O<sub>4</sub> shows the highest Seebeck coefficient (-514.539 μV/K) at 360 K as compared with the Ni-doped ZnFe<sub>2</sub>O<sub>4</sub>. For all studied compositions, as expected, the higher values of the Seebeck coefficient observed at room temperature are attributed to low carrier concentrations. The decreased values of Seebeck coefficient may also be possibly due to the filling up of oxygen vacancies and the migration of ions from one site to another site [29].

Fig. 7(c) depicts the change in power factor as a function of temperature for all the compositions. It is evident that power factor values of all the compositions increases with increase in temperature. Among the studied compositions Zn<sub>0.8</sub>Ni<sub>0.2</sub>Fe<sub>2</sub>O<sub>4</sub> shows the highest power factor 6.66 μW/mK<sup>2</sup> at 1048 K. By comparing Fig. 7(a) and (c), a direct correlation between electrical conductivity and power factor can also be observed here. When trivalent element Ni with ionic radii 0.55 Å is partially substituted at divalent Zn (0.6 Å) sites, the point defects thus generated will be donor sites supplying negative charge carriers to the crystal which will increase with the increase of Ni content and improve the conductivity at higher temperatures and thereby improve the thermoelectric properties and efficiency of the material. Another important

observation is that there is no significant difference in the room temperature electrical conductivities of all the three compositions. The substantial increment in electrical conductivity of the Ni doped samples with respect to increase in temperature indicates the importance of thermal activation in the conduction process.

As stated above, electron transport mechanism in spinel oxides is due to electron hopping between the cations in the octahedral site (B site) of the same element that exhibits more than one valence state [30]. To confirm the electron hopping behaviour, the electrical transport properties were studied in more detail. Fig. 8 depicts the variation of electrical conductivity  $\sigma$  with inverse temperature  $1000/T$ , which reveals the thermally activated electrical transport characteristics of material based on the Arrhenius equation (5).

$$\sigma = \sigma_0 \exp \frac{-E_a}{KT} \quad (5)$$

Where  $\sigma_0$  is the pre-exponential factor,  $E_a$  is the activation energy,  $K$  is the Boltzmann constant and  $T$  is the absolute temperature [31]. The experimental findings are in accordance with the Arrhenius law as revealed by their linear form with negative slope. It is observed from Fig. 8 that in all samples,  $\sigma$  decreases with the increase in temperature, indicating a negative temperature coefficient of resistance behaviour (NTCR), atypical characteristic feature of semiconducting materials [32]. Typically,  $E_a$  is the energy required to activate the charge carrier to overcome the potential barrier at the grain boundaries and take part in the conduction process. As the temperature increases, the electrons acquire sufficient amount of thermal energy to overcome the barrier. As observed from the previous characterisations, with the largest crystallite and grain size, highest carrier concentration and lowest mobility, undoped ZnFe<sub>2</sub>O<sub>4</sub> exhibits the highest activation energy value of  $1.18 \pm 0.06$ .  $E_a$  decreases with the doping of Ni, where the enhanced charge carrier hopping is expected due to the presence of multivalent Ni in some

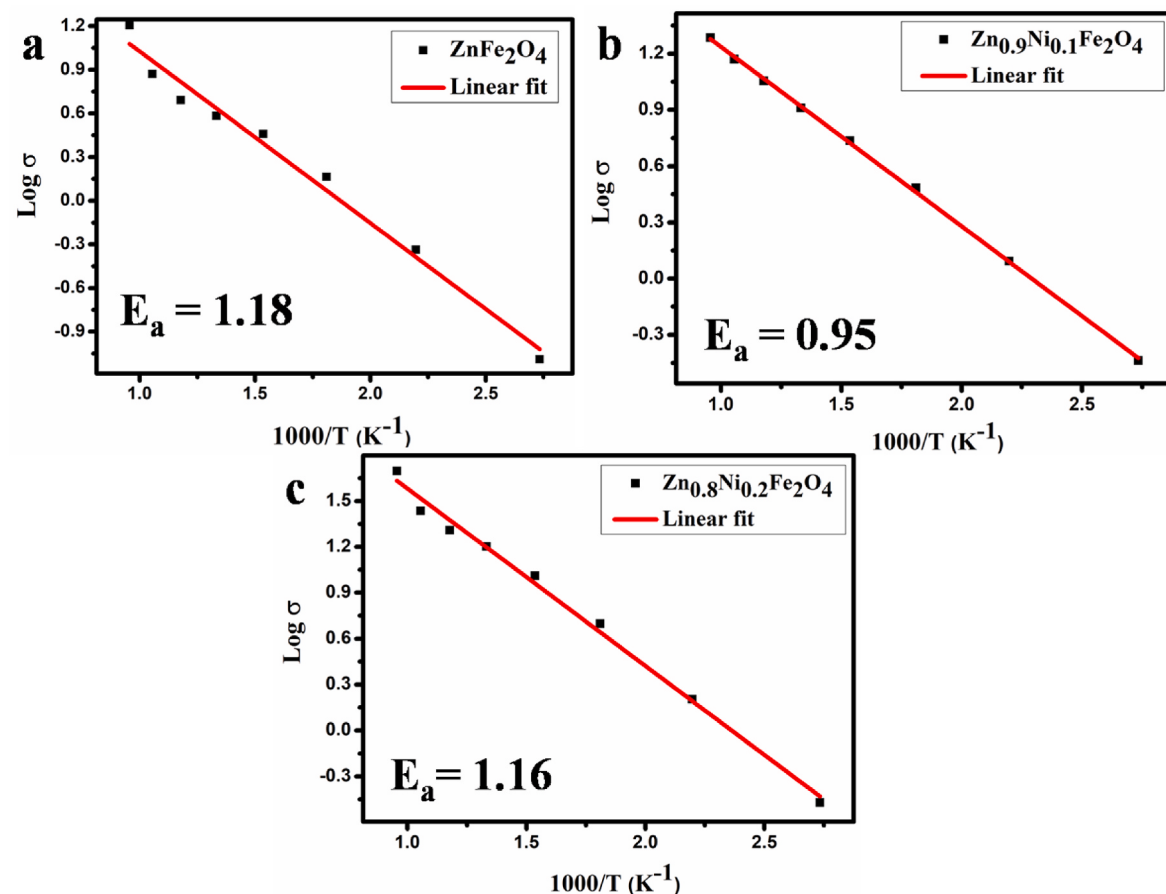


Fig. 8. Plot of  $\log \sigma$  vs.  $1000/T$  for  $Zn_{1-x}Ni_xFe_2O_4$  ( $0 \leq x \leq 0.2$ ) compounds.

of the Zn sites. The lowest  $E_a$  of  $0.95 \pm 0.008$  is exhibited by  $Zn_{0.9}Ni_{0.1}Fe_2O_4$ , which increases to  $0.16 \pm 0.03$  for  $Zn_{0.8}Ni_{0.2}Fe_2O_4$ , where the dopant concentration has reached its optimum value and further increase shows anomalous increase in resistivity.

Mott realized that  $n$  type semiconductors are regarded as Anderson insulators where electrons are concentrated in proximity to the fermi level and while receiving energy, electron could move from one site to another [33]. We examined the electron hopping conduction mechanism of  $Zn_{1-x}Ni_xFe_2O_4$  ( $0 \leq x \leq 0.2$ ) using Mott's variable range hopping model (VRH) and shown in equation (6). This model describes how temperature affects the hopping range and activation energy, such that hopping not only takes place among the vicinity of the neighbouring sites and also in another similar remote site which are often found to be non-Arrhenius [34].

$$\sigma = \sigma_0 \exp - \left\{ \frac{T_0}{T} \right\}^P \quad (6)$$

Where the  $\sigma$  and  $\sigma_0$  are conductivity and constant conductivity,  $T$  and  $T_0$  are the temperature and characteristic temperature constant, and  $P$  is the hopping dimension given by  $P = \frac{1}{n+1}$  where  $n$  is the hopping direction.

If the hopping direction is considered in all three dimensions; the value of  $P$  is  $\frac{1}{4}$ . It is assumed that hopping not only occurs in nearest neighbouring sites and also in three dimensions [35]. Fig. 9 depicts  $\log \sigma$  versus temperature ( $T^{-1/4}$ ) showing a linear relation, where  $\sigma$  directly depends on increase in temperature for all the studied compositions. The linear relation proves that the conductivity and ionic state of doped zinc ferrite mainly depends on hopping mechanism. The values of  $T_0$  derived from the slope of the  $\log \sigma$  vs.  $T^{-1/4}$  plot for  $ZnFe_2O_4$ ,  $Zn_{0.9}Ni_{0.1}Fe_2O_4$ , and  $Zn_{0.8}Ni_{0.2}Fe_2O_4$  are 4722, 3831 and 4644 K respectively. This value

of  $T_0$  is appropriate for the disordered  $n$  type semiconducting material [36]. Thus, we can see by comparing Figs. 8 and 9, the smallest activation energy in congruence with  $T_0$  value in the required range suggests that dominant conduction takes place through hopping mechanism of the charges near fermi level.

### 3.6. Thermal transport property of Ni-ZFO compounds

Temperature dependent thermal conductivities of  $ZnFe_2O_4$ ,  $Zn_{0.9}Ni_{0.1}Fe_2O_4$  and  $Zn_{0.8}Ni_{0.2}Fe_2O_4$  are shown in Fig. 10 (a). Thermal conductivity is one of the crucial characteristic that greatly influences the performance of thermoelectric material. As expected in the case of ceramics, a decrease in thermal conductivity with the increase in temperature is observed in all various compositions. At lower temperatures, the lowest thermal conductivity is exhibited by  $ZnFe_2O_4$ , with an increase with increasing Ni content. Similar trend was observed in room temperature carrier mobility indicating the contribution of electronic part in the total thermal conductivity. However, at elevated temperatures there is less difference in the total thermal conductivity values of doped and undoped ZFO.

Total thermal conductivity ( $\kappa_{tot}$ ) comprises electronic thermal conductivity ( $\kappa_e$ ) and lattice thermal conductivity ( $\kappa_l$ ). Electronic thermal conductivity is calculated using Wiedemann–Franz law, according to the relation shown in equation (7).

$$\kappa_e = L \sigma T \quad (7)$$

Where  $L$ ,  $\sigma$  and  $T$  represent Lorentz number, electrical conductivity and temperature respectively. From Fig. 10 (b) it is clear that electronic thermal conductivity increases with increase in temperature. It is evident that  $Zn_{0.8}Ni_{0.2}Fe_2O_4$  is showing higher electronic thermal

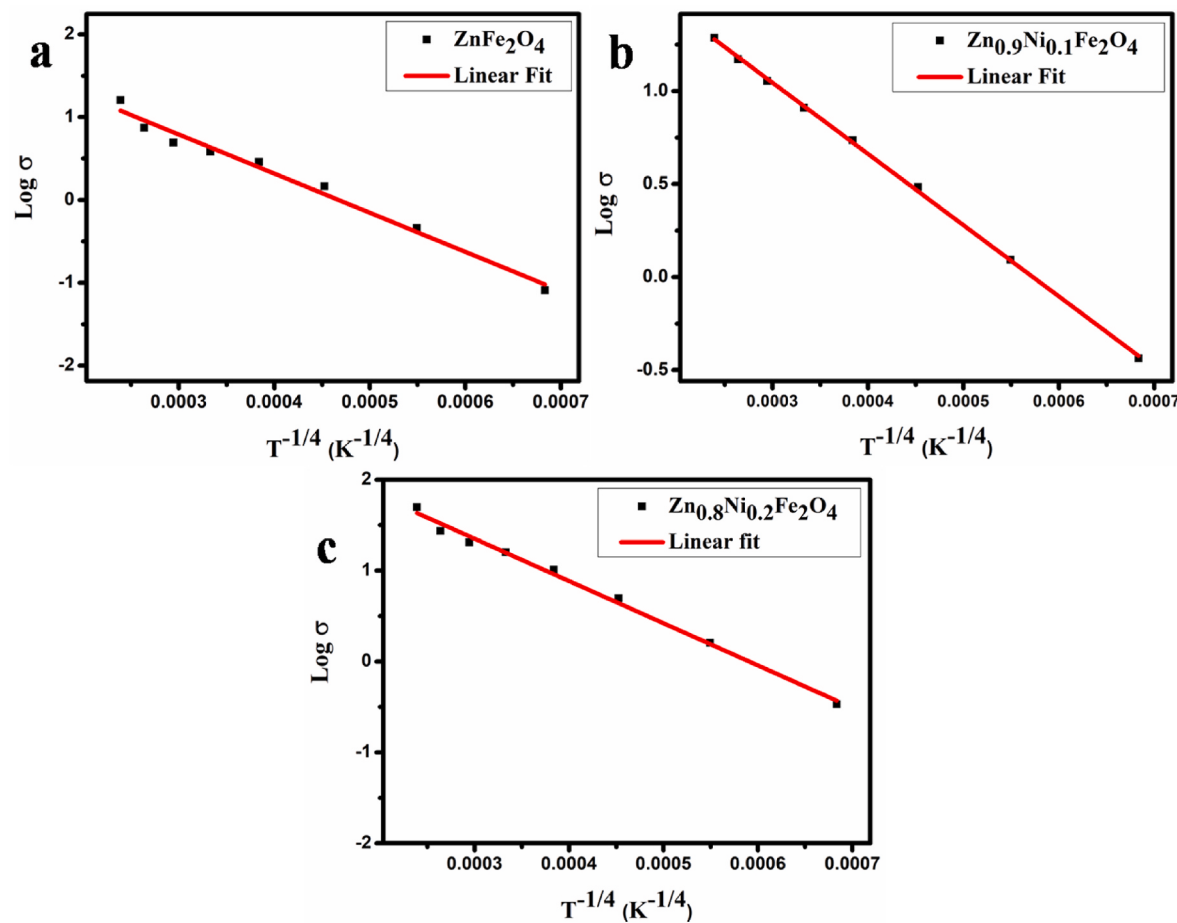


**Fig. 9.** Plot of Log  $\sigma$  vs.  $T^{-1/4}$  for  $Zn_{1-x}Ni_xFe_2O_4$  ( $0 \leq x \leq 0.2$ ) compounds.

conductivity in all studied temperature ranges. Doping has improved electrical conductivity and this directly contributes to an increase in electronic thermal conductivity.

For semiconductors, the lattice thermal conductivity ( $\kappa_l$ ) is calculated using equation (8) [37]

$$\kappa_{tot} = \kappa_e + \kappa_l \quad (8)$$

Where,  $\kappa_e$  and  $\kappa_{tot}$  is electronic thermal conductivity and total thermal conductivity respectively.

Fig. 10 (c) depicts the lattice thermal conductivity corresponding to  $ZnFe_2O_4$ ,  $Zn_{0.9}Ni_{0.1}Fe_2O_4$  and  $Zn_{0.8}Ni_{0.2}Fe_2O_4$ . It can be observed that electrons contribute much less to the total conductivity than phonons. In the studied temperature range, the lattice thermal conductivity increases with increase in dopant concentration. This is because the point defects generated due to the doping of Ni in Zn site effectively scatter phonons lowering lattice thermal conductivity. The lower crystallite and grain sizes of the doped compositions also significantly reduce the lattice thermal conductivity [38,39].

Thermoelectric figure of merit  $zT$  calculated based on the obtained parameters is shown in Fig. 10 (d). The graph depicts a uniform trend of increasing  $zT$  with respect to the temperature. Highest value of  $zT$  is obtained for  $Zn_{0.8}Ni_{0.2}Fe_2O_4$  ( $1.77 \times 10^{-2}$  at 1048 K) is so far the highest value reported for spinel ferrites. Other than this work it is reported that substitution of heterovalent  $Bi^{3+}$  at Co site of  $ZnCo_2O_4$  ( $ZnBi_{0.1}Co_{1.9}O_4$ ) exhibits the high  $zT$  of  $9.5 \times 10^{-4}$  at 668 K [40].

### 3.7. Electronic band structure

The electronic band structures were calculated after a variable-cell

relaxation (vc-relax) to obtain the optimized  $ZnFe_2O_4$  and Ni-doped  $ZnFe_2O_4$  structures shown in Fig. 11.

The electronic band structures of the  $ZnFe_2O_4$  and Ni-doped  $ZnFe_2O_4$  structures, displayed in Fig. 12, reveals a reduction in band gap with Ni doping as compared to the parent  $ZnFe_2O_4$ . This reduction in the band gap can be attributed to the shallow levels created by the doped Ni atoms [41].

The effective masses of electrons and holes, calculated following a parabolic fit to the CBM and VBM ( $1/m_e^* = (1/\hbar^2)\partial^2E/\partial k^2$ ), gradually goes up from  $0.90 m_0$  to  $1.24 m_0$  and  $2.63 m_0$  to  $2.88 m_0$  with Ni doping in  $ZnFe_2O_4$ , respectively.

Trivalent Ni in divalent Zn position added extra carriers in  $ZnFe_2O_4$ , being smaller in size than the host Zn ion, helped in enhancing the carrier mobility and also being multivalent, enhanced electron hopping thus achieving an overall increase in the electrical conductivity. In addition, being a point defect in the cationic sub lattice, Ni effectively reduced the lattice thermal conductivity at temperatures beyond 700°C, which is the suggested temperature range of application of this material. All these factors enhanced the thermoelectric properties of  $ZnFe_2O_4$  through enhancement in electrical conductivity, power factor and reduced thermal conductivity in the studied temperature range, with  $Zn_{0.8}Ni_{0.2}Fe_2O_4$  exhibiting the highest  $zT$ . The findings of this work validate that, similar to other oxide-based materials, spinel zinc ferrite exhibits promising features that can be significantly enhanced through doping, rendering it appropriate for use in high-temperature thermoelectric applications.

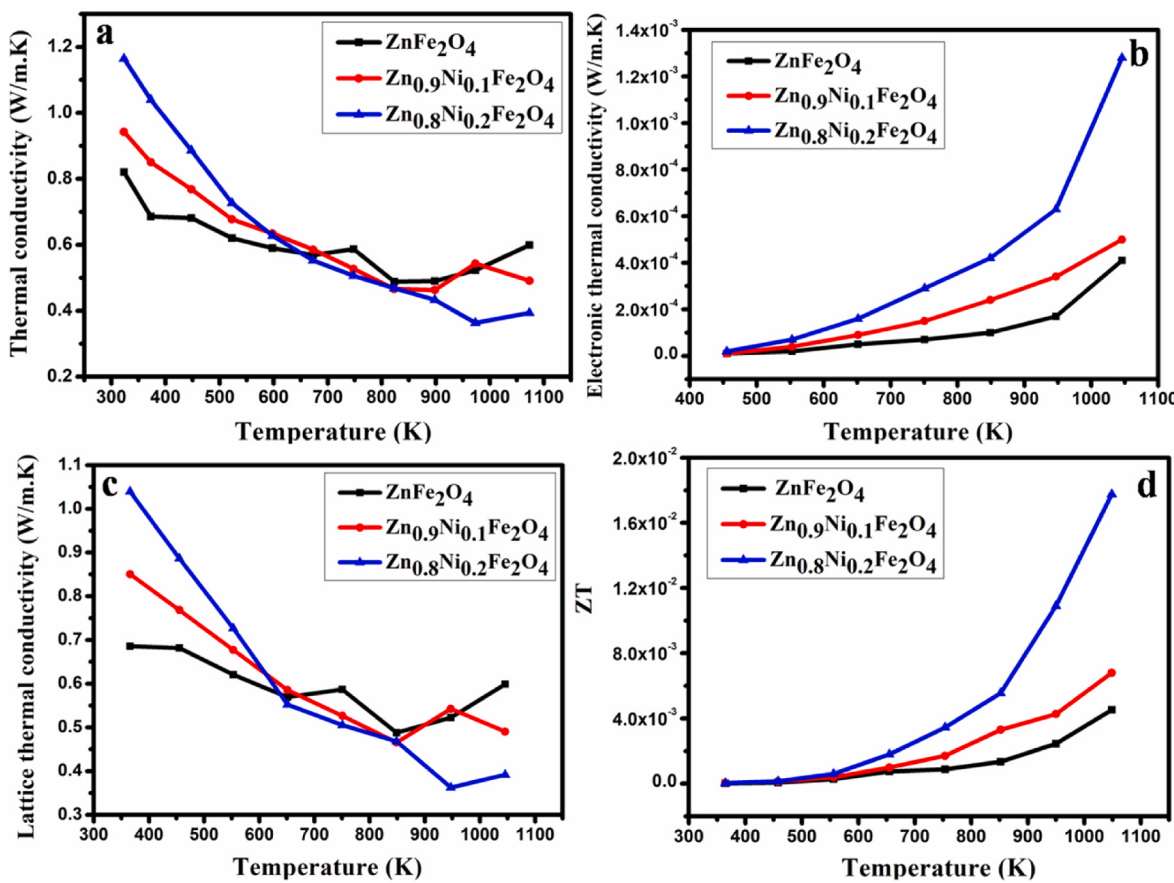


**Fig. 10.** (a) Total thermal conductivity, (b) Electronic thermal conductivity (c) Lattice thermal conductivity and (d) Figure of merit as a function of temperature of studied compounds.

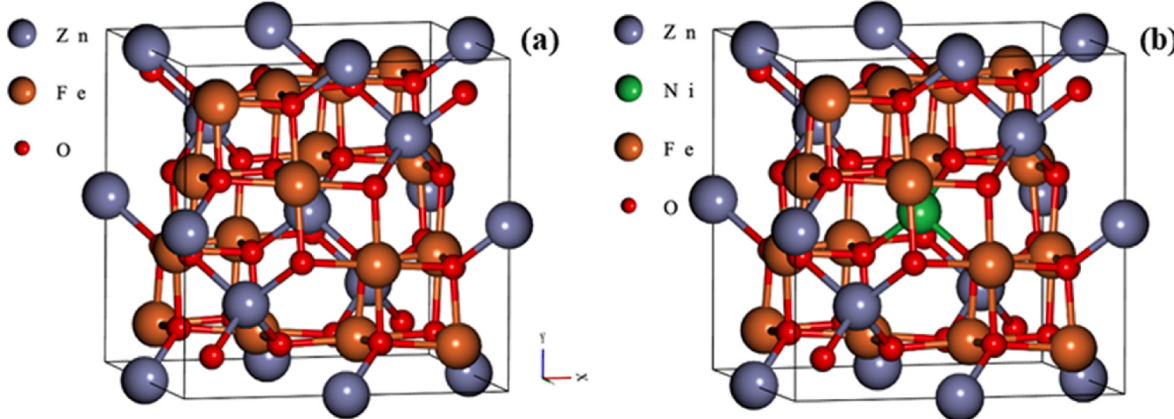


**Fig. 11.** The optimized structures of (a)  $\text{ZnFe}_2\text{O}_4$  and (b) Ni-doped  $\text{ZnFe}_2\text{O}_4$ .

#### 4. Conclusion

Spinel ferrite  $\text{Zn}_{1-x}\text{Ni}_x\text{Fe}_2\text{O}_4$  ( $0 \leq x \leq 0.2$ ) has been successfully synthesized via sol-gel method, followed by sintering in a reducing atmosphere. SEM images revealed that sintered pellets are composed of dense and compact grains with well-defined boundaries for all the compositions. HR-TEM shows the presence of discrete lattice fringes oriented across specific crystallographic planes, exhibiting the single crystalline nature of the individual particles. Investigation of electric transport properties demonstrated that the significantly enhanced electrical conductivity due to Ni doping is predominantly attributed to

the electron hopping between multivalent cations Fe and Ni.  $\text{Zn}_{0.8}\text{Ni}_{0.2}\text{Fe}_2\text{O}_4$  shows the maximum power factor of  $6.66 \mu\text{W}/\text{mK}^2$  and the highest figure of merit of  $1.77 \times 10^{-2}$  at 1048 K, which is so far the highest  $zT$  reported for any spinel ferrite. The present study scoops out the scope of spinel ferrite in the field of thermoelectrics, which has exceptional structural and electrical properties for high-temperature applications.

#### Declaration statement

During the preparation of this work the authors used Turnitin in

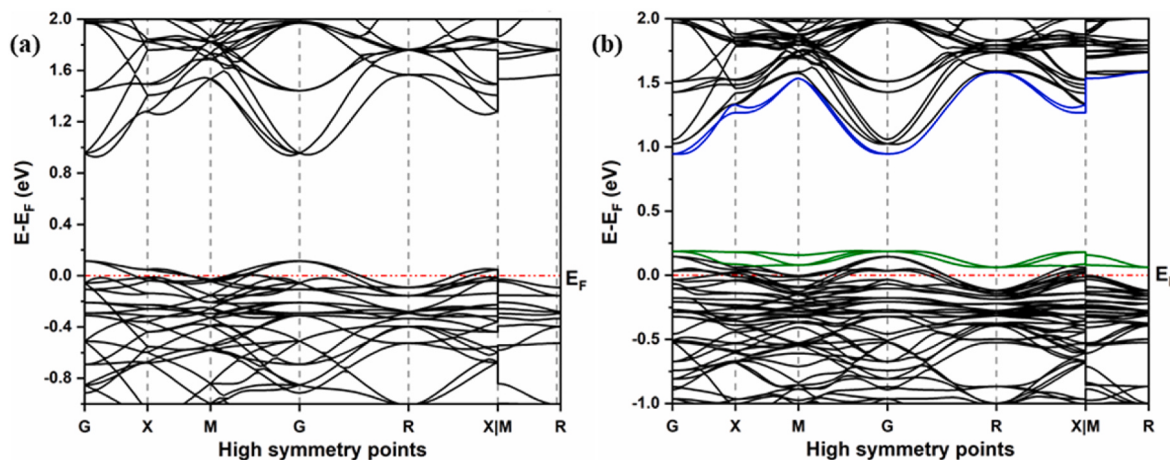


Fig. 12. The electronic band structures of  $\text{ZnFe}_2\text{O}_4$  and Ni-doped  $\text{ZnFe}_2\text{O}_4$  structures.

order to check plagiarism. After using this tool/service the authors reviewed and edited the content as needed and take full responsibility for the content of the publication.

#### CRediT authorship contribution statement

**Navya John:** Writing – original draft, Validation, Methodology, Conceptualization. **Nithya Davis:** Data curation. **T. Gokul Raja:** Resources. **J.C. Roshan:** Resources. **Shamima Hussain:** Funding acquisition. **Sebin Devasia:** Theoretical studies. **Bhuvanesh Srinivasan:** Resources. **Anuradha M. Ashok:** Validation, Supervision, Methodology, Funding acquisition, Conceptualization.

#### Declaration of competing interest

The authors declare that they have no known competing financial interests or personal relationships that could have appeared to influence the work reported in this paper.

#### Acknowledgements

The authors acknowledge the funding provided by UGC-DAE CSR through Collaborative Research Scheme (CRS) project number CRS/2021-22/04/612. The authors thank Mr. Venkatesan for the SEM characterisation of the samples. B.S. thanks the Science and Engineering Research Board (SERB) for the funding (File No. SRG/2023/002282) and IIT-Madras for the seed-grant (NFSG).

#### Appendix A. Supplementary data

Supplementary data to this article can be found online at <https://doi.org/10.1016/j.ceramint.2024.08.365>.

#### References

- [1] S.I. Kim, K. H Lee, H.A. Mun, H.S. Kim, S.W. Hwang, J.W. Roh, D.J. Yang, W. H. Shin, X.S. Li, Y.H. Lee, G.J. Snyder, S.W. Kim, Dense Dislocation Arrays Embedded in grain boundaries for high-performance Bulk thermoelectrics, *Sci* 348 (2015) 109–114, <https://doi.org/10.1126/science.aaa4166>.
- [2] Y. Pei, X. Shi, A. LaLonde, H. Wang, L. Chen, G.J. Snyder, Convergence of electronic bands for high performance Bulk thermoelectrics, *Nature* 473 (2011) 66–69, <https://doi.org/10.1038/nature09966>.
- [3] Z. Liu, J. Mao, T.H. Liu, G. Chen, Z. Ren, Nano-microstructural Control of phonon Engineering for thermoelectric energy Harvesting, *MRS Bull.* 43 (2018) 181–186, <https://doi.org/10.1557/mrs.2018.7>.
- [4] I. Terasaki, Y. Sasago, K. Uchinokura, Large thermoelectric power in  $\text{NaCo}_2\text{O}_4$  single crystals, *Phys. Rev. B* 56 (1997) R12685, <https://doi.org/10.1103/PhysRevB.56.R12685>.
- [5] R.V.R. Virtudazo, B. Srinivasan, Q. Guo, R. Wu, T. Takei, Y. Shimasaki, H. Wada, K. Kuroda, S. Bernik, T. Mori, Improvement in the thermoelectric properties of porous networked Al-doped ZnO Nanostructured materials synthesized via an Alternative Interfacial reaction and low-pressure SPS processing, *Inorg. Chem. Front.* 7 (2020) 4118–4132, <https://doi.org/10.1039/DQI00888E>.
- [6] M. Ohtaki, Oxide thermoelectric materials for heat-to-Electricity direct energy conversion, *Kyushu Univ. Glob. COE Progr. Nov., Carbon Resour. Sci. Newsl.* 3 (2010).
- [7] A.M. Ashok, Realization of high thermoelectric power factor in Ta-doped ZnO by grain boundary Engineering, *J. Appl. Phys.* 128 (2020), <https://doi.org/10.1063/5.0022287>.
- [8] B. Marfoua, J. Hong, Graphene Induced high thermoelectric performance in ZnO/graphene Heterostructure, *Adv. Mater. Interfaces.* 10 (2023) 2202387, <https://doi.org/10.1002/admi.202202387>.
- [9] N. Kumari, V. Kumar, S.K. Singh, Effect of  $\text{Cr}^{3+}$  substitution on properties of nano- $\text{ZnFe}_2\text{O}_4$ , *J. Alloys Compd.* 622 (2015) 628–634, <https://doi.org/10.1016/j.jallcom.2014.10.083>.
- [10] S. Xu, D. Feng, W. Shangguan, Preparations and Photocatalytic properties of Visible-Light-Active zinc ferrite-doped  $\text{TiO}_2$  Photocatalyst, *J. Phys. Chem. C* 113 (2009) 2463–2467, <https://doi.org/10.1021/jp806704y>.
- [11] G.Y. Zhang, Y.Q. Sun, D.Z. Gao, Y.Y. Xu, Quasi-cube  $\text{ZnFe}_2\text{O}_4$  Nanocrystals: Hydrothermal synthesis and Photocatalytic Activity with  $\text{TiO}_2$  (Degussa P25) as Nanocomposite, *Mater. Res. Bull.* 45 (2010) 755–760, <https://doi.org/10.1016/j.materresbull.2010.03.025>.
- [12] Y. Guo, N. Zhang, X. Wang, Q. Qian, S. Zhang, Z. Li, Z. Zou, A facile Spray Pyrolysis method to Prepare Ti-doped  $\text{ZnFe}_2\text{O}_4$  for Boosting photo electrochemical water Splitting, *J. Mater. Chem. A* 5 (2017) 7571–7577, <https://doi.org/10.1039/C6TA11134C>.
- [13] S.M. Masoudpanah, S.S. Ebrahimi, M. Derakhshani, S.M. Mirkazemi, Structure and magnetic properties of La substituted  $\text{ZnFe}_2\text{O}_4$  nanoparticles synthesized by sol-gel Auto combustion method, *J. Magn. Magn. Mater.* 370 (2014) 122–126, <https://doi.org/10.1016/j.jmmm.2014.06.062>.
- [14] R.C. O'handley, *Modern Magnetic Materials: Principles and Applications*, Wiley, 2000, p. 768.
- [15] T.A. Taha, S. Elrabaie, M.T. Attia, Green synthesis, structural, magnetic, and dielectric characterization of  $\text{NiZnFe}_2\text{O}_4/\text{C}$  Nanocomposite, *J. Mater. Sci. Mater. Electron.* 29 (2018) 18493–18501, <https://doi.org/10.1007/s10054-018-9965-4>.
- [16] A.H. Monfared, A. Zamani, M. Beygzedeh, I. Sharifi, M.A. Mozafari, Rapid and efficient thermal Decomposition Approach for the synthesis of Manganese-zinc/Oleyamine core/Shell ferrite nanoparticles, *J. Alloys Compd.* 693 (2017) 1090–1095, <https://doi.org/10.1016/j.jallcom.2016.09.253>.
- [17] J. Ma, X.X. Wang, G. Wang, H. Wang, Zinc ferrite Nanorod-Assembled Mesoporous Microspheres as Advanced anode materials for Sodium-ion Batteries, *Energy Technol.* 7 (2019) 1900479, <https://doi.org/10.1002/ente.201900479>.
- [18] H. Song, L. Zhu, Y. Li, Z. Lou, M. Xiao, Z. Ye, Preparation of  $\text{ZnFe}_2\text{O}_4$  Nanostructures and highly efficient Visible-Light-Driven hydrogen generation with the Assistance of nano heterostructures, *J. Mater. Chem. A* 3 (2015) 8353–8360, <https://doi.org/10.1039/C5TA00737B>.
- [19] G.K. Reddy, K. Gunasekara, P. Boolchand, P.G. Smirniotis, Cr-And Ce-doped ferrite Catalysts for the high temperature Water–gas shift reaction: TPR and Mossbauer spectroscopic study, *J. Phys. Chem. C* 115 (2011) 920–930, <https://doi.org/10.1021/jp102959p>.
- [20] Y. Ding, S. Tang, R. Han, S. Zhang, G. Pan, X. Meng, Iron oxides Nanobelt Arrays Rooted in Nanoporous surface of Carbon Tube Textile as Stretchable and Robust Electrodes for Flexible super capacitors with Ultrahigh areal energy density and remarkable Cycling-stability, *Sci. Rep.* 10 (2020) 11023, <https://doi.org/10.1038/s41598-020-68032-z>.
- [21] Y.S. Chen, J.F. Kang, B. Chen, B. Gao, L.F. Liu, X.Y. Liu, Y.Y. Wang, L. Wu, H.Y. Yu, E.G. Wang, Microscopic mechanism for Unipolar resistive Switching behaviour of nickel oxides, *J. Phys. D Appl. Phys.* 45 (2012) 065303, <https://doi.org/10.1088/0022-3727/45/6/065303>.

- [22] G.A. Alna'washi, A.M. Alsmadi, I. Bsoul, B. Salameh, G.M. Alzoubi, M. Shatnawi, S. M. Hamasha, S.H. Mahmood, Investigation on X-ray Photoelectron spectroscopy, structural and low temperature magnetic properties of Ni-Ti Co-substituted M-type Strontium Hexaferrites prepared by Ball Milling Technique, *Results Phys.* 28 (2021) 104574, <https://doi.org/10.1016/j.rinp.2021.104574>.
- [23] L. Han, X. Zhou, L. Wan, Y. Deng, S. Zhan, Synthesis of  $ZnFe_2O_4$  Nanoplates by Succinic acid-Assisted Hydrothermal route and their Photocatalytic Degradation of Rhodamine B under visible Light, *J. Environ. Chem. Eng.* 2 (2014) 123–130, <https://doi.org/10.1016/j.jece.2013.11.031>.
- [24] L. Zhang, T. Wei, J. Yue, L. Sheng, Z. Jiang, D. Yang, L. Yuan, Z. Fan, Ultra-small and highly Crystallized  $ZnFe_2O_4$  nanoparticles within double graphene networks for Super-Longlife Lithium-ion Batteries, *J. Mater. Chem. A*. 5 (2017) 11188–11196, <https://doi.org/10.1039/C7TA02726E>.
- [25] W. Kim, Strategies for Engineering phonon transport in thermoelectrics, *J. Mater. Chem. C* 3 (2015) 10336–10348, <https://doi.org/10.1039/C5TC01670C>.
- [26] S.A. Mazen, A. Elfalaky, Thermoelectric power and electrical conductivity of Cu-Ti ferrite, *J. Magn. Magn. Mater.* 195 (1999) 148–155, [https://doi.org/10.1016/S0304-8853\(98\)00348-5](https://doi.org/10.1016/S0304-8853(98)00348-5).
- [27] V.K. Lakhani, K.B. Modi, Effect of  $Al^{3+}$  substitution on the transport properties of Copper ferrite, *J. Phys. D Appl. Phys.* 44 (2011) 245403, <https://doi.org/10.1088/0022-3727/44/24/245403>.
- [28] B.R. Karche, B.V. Khasbardar, A.S. Vaingankar, X-ray, SEM and magnetic properties of MgCd ferrites, *J. Magn. Magn. Mater.* 168 (1997) 292–298, [https://doi.org/10.1016/S0304-8853\(96\)00705-6](https://doi.org/10.1016/S0304-8853(96)00705-6).
- [29] B.L. Patil, S.R. Sawant, S.S. Suryavanshi, S.A. Patil, Conduction mechanism in  $Sn^{4+}$  substituted Copper ferrite, *Bull. Mater. Sci.* 16 (1993) 267–271, <https://doi.org/10.1007/BF02746036>.
- [30] H. Eckert, C.J. Chen, M. Greenblatt, R.H. Herber, Electron hopping in Lithiated spinels: a temperature dependent Mössbauer study, *J. Phys. Chem. Solids.* 49 (1988) 71–77, [https://doi.org/10.1016/0022-3697\(88\)90137-0](https://doi.org/10.1016/0022-3697(88)90137-0).
- [31] J. Hou, R. Vaish, Y. Qu, D. Kršmanović, K.B.R. Varma, R.V. Kumar, Dielectric relaxation and electrical conductivity in  $Bi_5NbO_{10}$ Oxygen ion Conductors prepared by A Modified sol-gel process, *J. Power Sources* 195 (2010) 2613–2618, <https://doi.org/10.1016/j.jpowsour.2009.11.081>.
- [32] V. Khopkar, B. Sahoo, Low temperature dielectric properties and NTCR behavior of the BaFe 0.5 Nb 0.5 O 3 double perovskite ceramic, *Phys. Chem. Chem. Phys.* 22 (2020) 2986–2998, <https://doi.org/10.1039/C9CP05707B>.
- [33] N.F. Mott, Conduction in glasses containing transition metal ions, *J. Non-Cryst. Solids* 1 (1968), [https://doi.org/10.1016/0022-3093\(68\)90002-1](https://doi.org/10.1016/0022-3093(68)90002-1).
- [34] N.F. Mott, E.A. Davis, *Electronic Properties in Non-crystalline Materials*, Clarendon Press, Oxford, U.K., 1971.
- [35] B.I. Shklovskii, A.L. Efros, *Electronic Properties of Doped Semiconductors*, Springer Science & Business Media, 2013.
- [36] A. Yildiz, N. Serin, T. Serin, M. Kasap, Crossover from nearest-Neighbour hopping conduction to Efros-Shklovskii variable-range hopping conduction in Hydrogenated Amorphous Silicon Films, *Jpn. J. Appl. Phys.* 48 (2009) 111203, <https://doi.org/10.1143/JJAP.48.111203>.
- [37] F. Li, J.F. Li, J.H. Li, F.Z. Yao, The effect of Cu substitution on Microstructure and thermoelectric properties of  $LaCo_3O_3$  ceramics, *Phys. Chem. Chem. Phys.* 14 (2012) 12213–12220, <https://doi.org/10.1039/C2CP41743J>.
- [38] D. Chen, Y. Zhao, Y. Chen, B. Wang, H. Chen, J. Zhou, Z. Liang, One-step chemical synthesis of  $ZnO$ /graphene oxide molecular Hybrids for high-temperature thermoelectric applications, *ACS Appl. Mater. Interfaces* 7 (2015) 3224–3230, <https://doi.org/10.1021/am507882f>.
- [39] R.V. Virtudazo, Q. Guo, R. Wu, T. Takei, T. Mori, An Alternative, Faster and Simpler method for the formation of Hierarchically porous  $ZnO$  Particles and their thermoelectric performance, *RSC Adv.* 7 (2017) 31960–31968, <https://doi.org/10.1039/C7RA05067D>.
- [40] A.A. Nedunchezian, D. Sidharth, R. Rajkumar, N.Y. Devi, K. Maeda, M. Arivanandan, K. Fugiwara, G. Anbalagan, R. Jayavel, Enhancing the thermoelectric power factor of Nanostructured  $ZnCo_2O_4$  by Bi substitution, *RSC Adv.* 10 (2020) 18769–18775, <https://doi.org/10.1039/DORA01542C>.
- [41] P. Giannozzi, S. Baroni, N. Bonini, M. Calandra, R. Car, C. Cavazzoni, R. M. Wentzcovitch, Quantum ESPRESSO: a modular and open-source software project for quantum simulations of materials, *J. Phys. Condens. Matter* 21 (39) (2009) 395502, <https://doi.org/10.1088/0953-8984/21/39/395502>.